

# Directional amorphization of boron carbide subjected to laser shock compression

Shiteng Zhao<sup>a</sup>, Bimal Kad<sup>a</sup>, Bruce A. Remington<sup>b</sup>, Jerry C. LaSalvia<sup>c</sup>, Christopher E. Wehrenberg<sup>b</sup>, Kristopher D. Behler<sup>c</sup>, and Marc A. Meyers<sup>a,1</sup>

<sup>a</sup>University of California, San Diego, La Jolla, CA 92093; <sup>b</sup>Lawrence Livermore National Laboratory, Livermore, CA 94550; and <sup>c</sup>United States Army Research Laboratory, Aberdeen Proving Ground, Aberdeen, MD 21005

Edited by David A. Weitz, Harvard University, Cambridge, MA, and approved September 13, 2016 (received for review March 23, 2016)

**Solid-state shock-wave propagation is strongly nonequilibrium in nature and hence rate dependent. Using high-power pulsed-laser-driven shock compression, unprecedented high strain rates can be achieved; here we report the directional amorphization in boron carbide polycrystals. At a shock pressure of 45~50 GPa, multiple planar faults, slightly deviated from maximum shear direction, occur a few hundred nanometers below the shock surface. High-resolution transmission electron microscopy reveals that these planar faults are precursors of directional amorphization. It is proposed that the shear stresses cause the amorphization and that pressure assists the process by ensuring the integrity of the specimen. Thermal energy conversion calculations including heat transfer suggest that amorphization is a solid-state process. Such a phenomenon has significant effect on the ballistic performance of B<sub>4</sub>C.**

lasers | shock wave | amorphization | boron carbide

**B**oron carbide is one of the hardest materials on earth while extremely lightweight, making it excellent for ballistic protection applications such as body armor (1–6). Thus, its dynamic behavior under impact/shock loading has been the subject of intensive studies for decades (1, 5–13). It is known that boron carbide undergoes an abrupt shear strength drop at a critical shock pressure around 20~23 GPa, suggesting a deteriorated penetration resistance (8). Based on similar observations in geological materials (5), Grady (7) hypothesized that this was caused by localized softening mechanisms such as shear localization and/or melting. Examining fragments collected from a ballistic test using transmission electron microscopy (TEM), Chen et al. (14) were the first to identify localized amorphization in boron carbide, which appeared to be aligned to certain crystallographic planes. However, because the loading history of these fragments is unknown, its effect on the observed microstructure is not understood. Additionally, although the more well-defined loading conditions associated with quasi-static diamond-anvil cell (15) and nano-indentation (16, 17) experiments have provided greater insight into amorphization of boron carbide, they do not address the regime of high strain rate.

The laser shock experimental technique offers promise in bridging the gaps of the previous experiments by enabling boron carbide to be shock compressed under controlled and prescribed uniaxial strain loading conditions and then recovered for postshock characterization by TEM. To ensure the integrity of the specimen, the duration of the stress pulse should be smaller than the characteristic time for crack propagation which is typically on the microsecond scale [limited by Rayleigh wave speed (18)]. Traditional dynamic loading methods such as plate impact and split Hopkinson bar cannot deliver the strain rates required because the stress pulses of both techniques occur on microsecond time scales. Therefore, brittle solids such as B<sub>4</sub>C will fail catastrophically by crack nucleation, propagation, and coalescence (19). To solve this challenge, we designed a laser shock-recovery experimental apparatus which was implemented in the Jupiter Laser Facility (Janus), Lawrence Livermore National Laboratory. The Janus laser is capable of generating large-amplitude stress pulses with nanosecond duration,

sufficient to shock boron carbide above its amorphization threshold and to prevent it from shattering under shock compression and release. The high-energy pulsed laser (nominal wavelength = 528 nm, laser energy = 50 J) has a nominal square pulse shape with duration of 3 ns, resulting in a pulse power of 1.67 TW/cm<sup>2</sup>. Such a high energy density was deposited onto a target package which comprised aluminum foil (200 μm) placed in front of a B<sub>4</sub>C polycrystal (3 mm in diameter and 3 mm in height, Fig. 1A). The vaporization of the Al foil provides the high pressure which drives the shock wave into B<sub>4</sub>C. Titanium capsule and momentum trap are used to capture the reflected tensile stress pulses. The peak shock pressure (45~50 GPa) can be determined by a separate velocity interferometer system for any reflector (VISAR) experiment (Fig. 1B–D) and subsequent impedance matching (Fig. 1E) (20), which is detailed in *Methods*. Successful recovery experiments enable examination of the microstructure of the shocked boron carbide right below the shock surface.

The shock-recovered microstructure is shown in the low-magnification bright-field TEM image in Fig. 2A. A crack extending into the sample from the shock surface, as well as multiple subsurface planar faults, can be clearly seen. The crack is oriented 45° from the shock direction, coinciding with the maximum shear direction. The planar faults appear to be nominally parallel to the maximum shear orientation, although deviations of ~15° are noted. The specific orientation of individual grains and crystallographic requirements undoubtedly determine the orientation of the planar faults. The near alignment with the maximum shear direction indicates the important role that shear stress plays in their formation. These planar faults lead to lattice misalignment, accommodated by lattice shifts (marked by red triangles) in the surrounding region, which are observed by the high-resolution TEM (HRTEM) image shown on zone [1̄51]\* in Fig. 2B (“b” region in Fig. 2A) (21). The Fourier filtered lattice fringes [using (101) Bragg reflection] of the dislocated

## Significance

**When crystalline solids are stressed quasi-statically, dislocation slip, twinning, and phase transformations are the predominant mechanisms to dissipate the imparted elastic energy. Under shock, high hydrostatic and shear stresses promptly build up at the shock front, favoring fast energy dissipation mechanisms. Amorphization, which may only involve localized atomic arrangements, is therefore an additional potential candidate. Shock-induced amorphization has now been reported in various materials and hence should be incorporated as a deformation/damage mechanism of crystals subjected to high-strain-rate loading.**

Author contributions: B.A.R. and M.A.M. designed research; S.Z. and C.E.W. performed research; S.Z., B.K., J.C.L., and K.D.B. analyzed data; K.D.B. provided materials; and S.Z. wrote the paper.

The authors declare no conflict of interest.

This article is a PNAS Direct Submission.

<sup>1</sup>To whom correspondence should be addressed. Email: mameyers@eng.ucsd.edu.

This article contains supporting information online at [www.pnas.org/lookup/suppl/doi:10.1073/pnas.1604613113/-DCSupplemental](http://www.pnas.org/lookup/suppl/doi:10.1073/pnas.1604613113/-DCSupplemental).

\*Crystal planes and directions are given adopting the hexagonal crystal representation for boron carbide and using Miller indices notation.

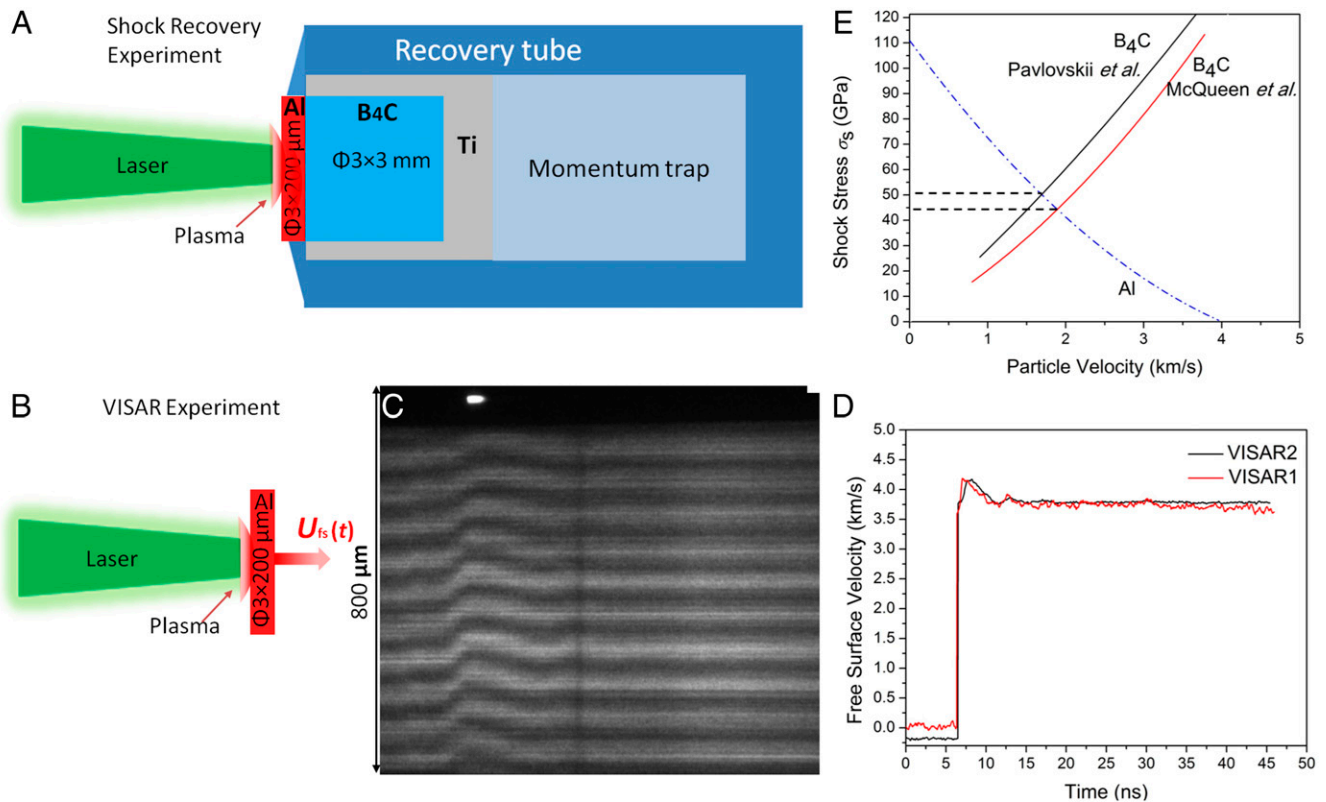


**Fig. 1.** Laser shock-recovery assembly, free-surface VISAR, and determination of shock parameters. (A) Schematic drawings of the shock-recovery experiment and (B) VISAR experiment. (C) Temporally resolved VISAR fringes, showing the shock break-out and pull-back features. (D) Free-surface velocity,  $U_{fs}$  vs.  $t$  profiles. Two independent VISAR channels with distinctive Etalon length were used to unambiguously determine the free-surface velocity. Peak  $U_{fs} \sim 4.2$  km/s, rendering  $U_p \sim 1/2 U_{fs} = 2.1$  km/s. (E) Determination of shock stress by impedance match shock Hugoniot ( $\sigma_s$  vs.  $U_p$ ) of aluminum and boron carbide. At the interface of Al and boron carbide, shock wave is reflected and the shock pressure changes as equilibrium is reached. The inverted shock Hugoniot of Al gives the estimate of the reflected curve (blue). Intersection of the reflected Al curve with shock Hugoniot of boron carbide yields the estimate of the shock pressure in boron carbide. Taking  $U_p = 2.1$  km/s from D, one obtains shock stress,  $\sigma_s = 45\text{--}50$  GPa, according to two most representative boron carbide Hugoniots from Pavlovskii (5) and McQueen et al. (6), respectively.

region in Fig. 2B are shown in Fig. 2C where disregistry of lattice can be observed. Geometric phase analysis of the same region is performed and the deviatoric strain field (as illustrated in Fig. 2D) in the vicinity of the planar fault is significantly higher than in the matrix (22). These planar faults are plausibly the precursors or the early stage of amorphization; however, whether they are amorphous is unclear at this point.

Amorphous bands can be observed a few micrometers below the shock surface. These bands (a-B<sub>4</sub>C in Fig. 3), unlike those observed in similar experiments performed on silicon (23, 24), do not necessarily originate from the shock surface and appear to terminate within the crystal, resulting in an ellipsoidal shape as shown in Fig. 3A. The diffuse ring in the fast Fourier transformed (FFT) diffractograph shown in Fig. 3C confirms the amorphous structure of these bands. The nominal widths of the amorphous “ellipsoids” range from 2 to 5 nm. In the vicinity of the tips of these bands, rotation of the lattice is clearly visible, as shown in Fig. 3B (misorientation of 6°). The lattice rotation is consistent with the first observations by Chen et al. (14). The zone axis is [713] and the amorphous band aligns roughly with the (215) plane. It is difficult to establish the amorphous plane and the assumption that it is normal to the TEM foil is made. Geometric phase analysis based on Fig. 3C is presented in Fig. 3D where the deviatoric strain within the amorphous region is much greater than its surrounding. Another amorphous band aligning roughly with (221) has been identified (as shown in *SI Appendix*, Fig. S4), indicating that amorphization depends on the orientation of the specific grain with respect to the shock wave propagation orientation.

Some bands are contiguous with cracks; this represents a clear connection between amorphization and the increase in fragmentation originally observed by Moynihan et al. (25) in boron carbide impacted ballistically above a critical shock pressure. However, it is also evident that the planar faults and amorphous bands are not always contiguous with cracks, but are distributed randomly in the sample. The ultrashort stress pulse duration (tens of nanoseconds including the shock release) is at least an order of magnitude smaller than the characteristic time (microseconds) for crack propagation, effectively preventing the sample from catastrophic failure (comminution).

Under shock compression (uniaxial strain) below the Hugoniot elastic limit (HEL) and for a shock wave propagating in the  $x_3$  direction, the generalized Hooke’s law simplifies to

$$\sigma_{ij} = C_{ijkl}\epsilon_{kl} = C_{ij33}\epsilon_{33}, \quad [1]$$

where  $C_{ijkl}$  is the fourth-order elastic constant (stiffness) tensor and  $\epsilon_{33}$  is the uniaxial strain aligned with direction of shock wave propagation. Therefore, the maximum shear stress,  $\tau_{\max}$ , and hydrostatic pressure,  $P$ , are functions of elastic constants and longitudinal strain, and can be written as

$$\frac{\tau_{\max}}{P} = \frac{3(C_{33} - \min\{C_{13}, C_{23}\})}{2(C_{33} + C_{13} + C_{23})}, \quad [2]$$

where the stiffnesses are represented in the matrix (two-index) notation. For boron carbide, with a low-symmetry rhombohedral

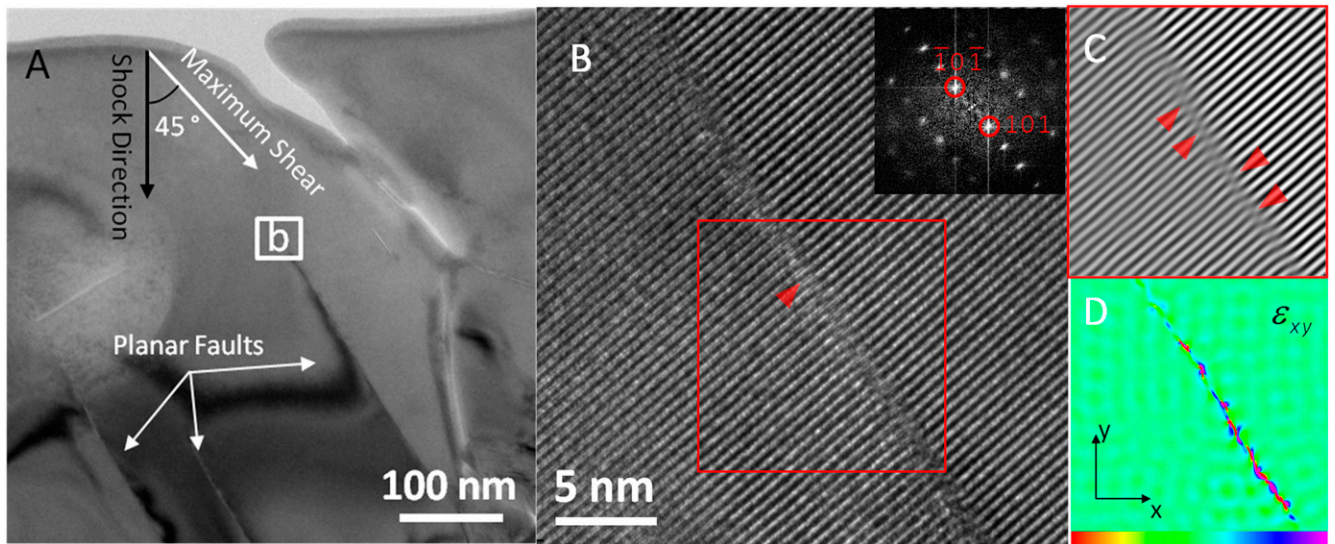


**Fig. 2.** TEM/HRTEM micrographs of recovered boron carbide from laser shock compression. (A) Low-magnification TEM image shows the shocked surface with crack in the center. (B) Planar fault can be identified and HRTEM image shows successive lattice disregistries (marked by red triangles) lying along the interface. (C) The Fourier filtered image of the boxed region in B, using (101) and  $(\bar{1}0\bar{1})$  reflections. (D) Corresponding geometric phase analysis shows the deviatoric strain field in the vicinity of the planar fault.

lattice (26), different structure models predict different values. Using ab initio simulation, Aryal et al. (27) calculated values of  $C_{33} = 553.1$  GPa and  $C_{13} = 76.8$  GPa; ignoring the small difference between  $C_{13}$  and  $C_{23}$ , Eq. 1 simplifies to

$$\frac{\tau_{\max}}{P} = \frac{3(C_{33} - C_{13})}{2(C_{33} + 2C_{13})} \approx 1, \quad [3]$$

indicating that the shear stress in boron carbide before the onset of inelastic deformation is very significant.

The shock stress is related to hydrostatic and deviatoric stresses by,  $\sigma_s = P + (4/3)\tau_{\max}$ . Thus, at HEL [ $\sigma_s \sim 20$  GPa (11, 28)],  $\tau_{\max} \approx P = 8.6$  GPa. In the laser shock experiment, the shock pressure,  $\sigma_s = 45 \sim 50$  GPa, is much higher than the HEL, and it is expected that the shear stress will be relaxed by directional amorphization. It should be noted that boron carbide is a strongly anisotropic material (with anisotropy ratios of  $C_{33}/C_{11} = 0.98$ ,  $C_{13}/C_{12} = 0.49$ ,  $2C_{44}/(C_{11} - C_{12}) = 0.8$ ), and, as a result,  $E_{\max}/E_{\min} = 8.1$  (29). To determine the stress state on a specific plane, Voigt's approach to coordinate transformation on stiffness tensor needs to be performed before the calculation of the Cauchy normal and shear stresses (30). If  $C_{ijkl}$  is the original stiffness tensor, one can write

$$C_{mnop} = l_{mi}l_{nj}l_{ok}l_{pl}C_{ijkl}, \quad [4]$$

where  $C_{mnop}$  is the stiffness tensor in the new coordinate system and  $l$  are the direction cosines. The ratios between the resolved shear stress  $\tau$  and shock stress  $\sigma_s$  on the observed planar fault (as in Fig. 2) and amorphous band (as in Fig. 3) are 0.25 and 0.2, respectively. Therefore, the amorphization process is strongly loading-path dependent. The detailed coordination transformation can be found in *SI Appendix*. Amorphization is promoted by shear deformation because it gives rise to larger lattice displacements than those by hydrostatic pressure.

Pressure may also play a role in amorphization of  $B_4C$ . It was shown that  $B_4C$  exhibits a negative melting slope with  $dT/dP \approx -13 \pm 6$  K/GPa (31), resulting in a reduction of melting temperature up to 200 K at the HEL ( $\sim 20$  GPa). Besides, the elastic stiffness of boron carbide is pressure dependent, indicating

that pressure may affect the shear instability of  $B_4C$ , the dominant amorphization mechanism.

The increase in temperature due to shock compression can be evaluated from the Hugoniot relations and experimentally determined shock parameters. This is shown in Fig. 4 (marked as homogeneous shock temperature,  $T_{\text{homo}}$ ), in conjunction with the decrease of melting point. Clearly,  $T_{\text{homo}}$  is not sufficient for melting at a shock stress of 45 GPa.

In addition to the  $T_{\text{homo}}$ , there is localized heat generation because of the lattice friction associated with shear localization. It is assumed that shear localization and amorphization start at HEL. The localized temperature rise  $\Delta T_{\text{band}}$  in an amorphous band of width  $w_{\text{band}}$  can be estimated by assuming that the relaxation in deviatoric strain energy is balanced by the increase in internal energy and heat transfer to its surroundings. The heat extracted from the shear band is modeled assuming that there is a constant heat generation in its symmetry plane, a problem that was solved analytically by Carslaw and Jaeger (32, 33) assuming a semi-infinite body on whose surface heat is deposited (more details in *SI Appendix*),

$$\Delta T_{\text{band}} = \frac{2}{\sqrt{\pi}} \frac{\beta \tau \gamma w_{\text{band}}}{\Delta t} \sqrt{\frac{t}{k \rho C_p}}, \quad [5]$$

where  $\beta$  is the fraction of deviatoric strain energy converted to thermal energy (usually taken as 0.9),  $k$  is thermal conductivity,  $\tau$  and  $\gamma$  are the shear stress and strain inside the band, respectively. The former is approximated as  $\tau_{\max}$  at HEL, and assumed to be independent of increasing shock stress. The latter is related to the uniaxial strain ( $\epsilon_{\text{uniaxial}}$ ), width ( $w_{\text{band}}$ ), and interspacing ( $w_{\text{spacing}}$ ) of bands,  $\gamma \approx \epsilon_{\text{uniaxial}}(w_{\text{spacing}}/w_{\text{band}} + 1)$ , if all of the deviatoric strain is relaxed by shear band.  $w_{\text{band}} = 2 \sim 10$  nm can be measured from postmortem TEM micrographs and  $w_{\text{spacing}} \sim 1$   $\mu\text{m}$  is approximated as the particle size because typically there is only one amorphous band per grain.

Fig. 4 plots  $\Delta T_{\text{band}}$  with varying  $\beta$  at time  $t = 3$  ns which is approximated as the laser pulse duration  $\Delta t$ . The uncertainties in Eq. 5 render the accuracy of prediction heavily dependent on these material parameters, especially the strain in the amorphous band and flow-stress dependence of strain softening. In the case

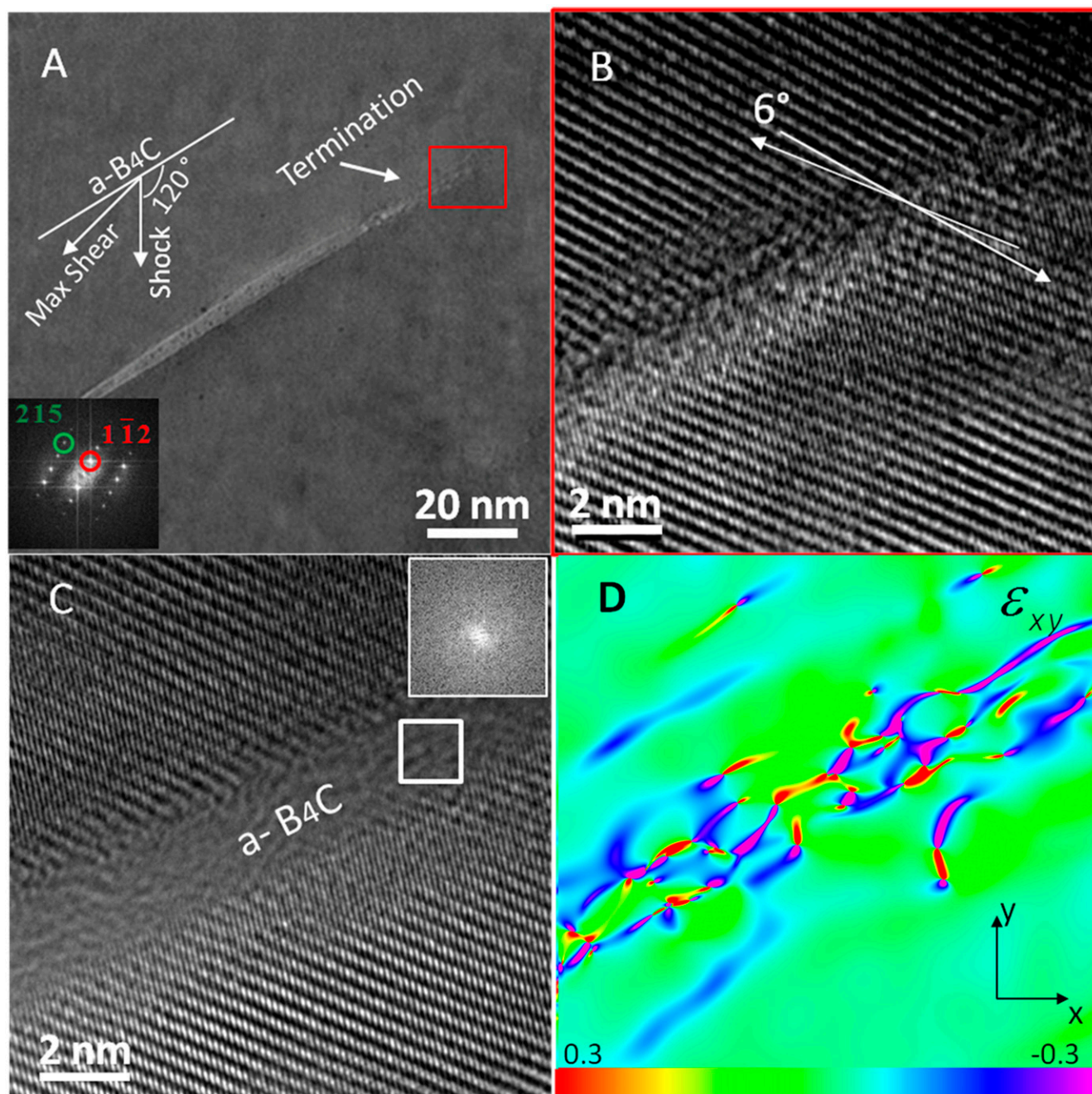


**Fig. 3.** HRTEM micrographs of amorphous band far away from the crack. (A) Both ends of the amorphous band, which exhibits an ellipsoidal shape, terminate in material (one end is shown here). (B) Lattice image at the tip of the amorphous band shows clear lattice rotation. (C) Lattice image showing the amorphous region (marked as a-B<sub>4</sub>C) with inset showing the corresponding FFT diffractograph. (D) Geometrical phase analysis corresponding to C shows that the local shear strain ( $\epsilon_{xy} = (1/2)\gamma$ ) is significantly higher in the amorphous region than its surroundings, indicating that shear stress plays a crucial role in amorphization.

of softening, the temperature rise will be decreased. Nevertheless, the physical picture qualitatively captured in Eq. 5 provides an estimate for localized heating. Although the prediction is clearly below the melting point at the pressure, it is possible that localized melting might occur. Thermal fluctuations and “hot spots” have been observed along shear bands in metals. The localized heating may also lead to formation of nanocrystals in the vicinity of the stress concentration (crack), as evidenced in *S1 Appendix, Fig. S3*.

Several atomistic mechanisms have been proposed to explain how B<sub>4</sub>C amorphizes under external loading: (i) Destruction

of C–B–C chain (34), (ii) transformation into and then collapse of B<sub>12</sub>–CCC polytype (35), (iii) break of boron–carbon bonds between neighboring icosahedra (36), (iv) depressurization amorphization (15). These mechanisms suggest that the icosahedra remain intact under stresses, whereas (v) recently An and Goddard (3) performed large-scale reactive-force-field molecular dynamics simulations and proposed that the fracture of the icosahedra also contributes to amorphization. The observations shown in this study cannot distinguish among the reported mechanisms, which may coexist in experiments depending on the loading path.

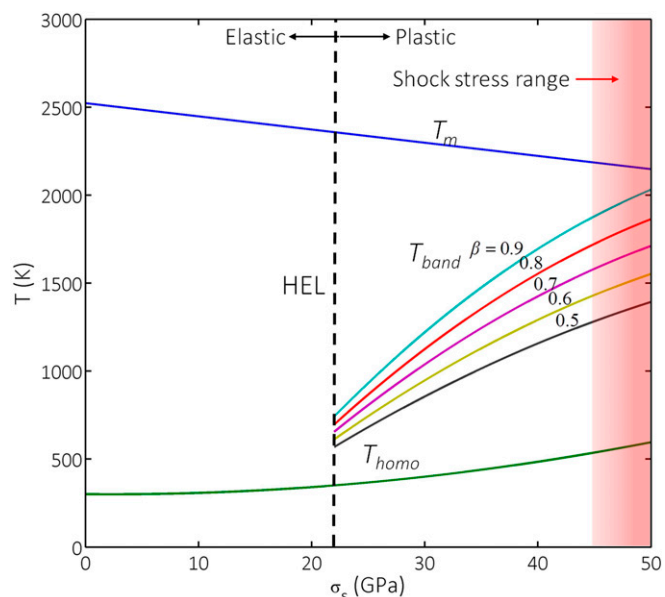


**Fig. 4.** Homogeneous and localized temperature rise as a function of shock compression. The applied shock pressure of 45–50 GPa is significantly below the pressure for homogeneous shock-induced melting ( $T_{homo}$ ), although the melting temperature  $T_m$  decreases as pressure increases. Conversion of strain energy inside the amorphization band to heat generated by shear leads to localized temperature increase  $\Delta T_{band}$ . Different values of heat conversion factor  $\beta$  are assumed. Note that the localized temperature rise only occurs in the plastic regime ( $\sigma_s > HEL$ ). The calculation represents an estimate and incorporates heat extraction from the band; no melting is predicted.

Despite the complicated nature of atomic displacements during amorphization, it is clear that shear stresses are vital to the process. They lead to large magnitude atomic displacements which can be dissipated by amorphization, cleavage, and dislocation/twin formation. These mechanisms compete in  $B_4C$  under shock loading; however, as the strain rate increases, amorphization is kinetically favored, suggesting a transition of failure mode from crack nucleation/propagation to amorphization. The exact threshold for amorphization in the laser-shocked  $B_4C$  is unknown but the 25-GPa shock experiment does not generate amorphous

bands. Thus, amorphization initiates somewhere between 25 and 50 GPa, which is higher than the previous report of 23.3 GPa for the long-pulse shock experiment by Chen and coworkers (13). This is consistent with first-order phase transitions, which are time dependent. The amorphization significantly influences the equation of state and shock Hugoniot of boron carbide. At this point, it is unclear whether unloading will modify the deformation microstructure. Further large-scale molecular dynamic simulation might shed more light on this process.

## Methods

**Laser-Recovery Experiment.** Laser-driven shock-recovery experiments were conducted at the Jupiter Laser Facility (Janus), Lawrence Livermore National Laboratory. Such high-energy density, once deposited onto the target, ablates its surface and creates a shock wave that propagates through the target. The ablation pressure is proportional to the laser intensity to 2/3 power. The experimental setup is shown in Fig. 1A. The aluminum foil has three functions: (i) as an ablator to transform laser energy into stress pulse; (ii) as a heat shield which minimizes the preheating induced by laser irradiation; (iii) as a pulse shaper to render the shock pulse on the target surface planar (uniaxial strain condition).

**VISAR Experiment and Impedance Matching.** In a separate shot, the rear (free-) surface velocity of the free standing aluminum foil subjected to a similar laser shock is characterized by VISAR, which is shown in Fig. 1B and C. The free-surface velocity ( $U_f$ ) can be approximated as twice of the particle velocity ( $U_p$ ):  $U_p \sim 0.5 U_f$ . Conservation of momentum gives the relationship between the initial density  $\rho_0$ , particle velocity  $U_p$ , shock velocity  $U_s$ , and longitudinal stress or shock pressure,  $\sigma_s$ , as  $\sigma_s = \rho_0 U_s U_p$ . The shock pressure on the surface boron carbide is determined by shock impedance  $Z$  [ $Z = \rho_0 U_s$  (20)] matching, as can be seen in Fig. 1E (Inset), which shows the target package of the recovery experiment. The shock Hugoniot data for Al are well characterized and documented by Los Alamos National Laboratory SESAME database (37). For boron carbide there are some discrepancies among the data reported in the literature (9), depending on the initial porosity of the materials. Two most representative Hugoniots by Pavlovskii (5) and McQueen et al. (6) were used.

**ACKNOWLEDGMENTS.** The enthusiastic help by Dorothy Coffey and Karren More is gratefully acknowledged. We acknowledge the highly professional support team of the Jupiter Laser Facility at Lawrence Livermore National Laboratory. Electron microscopy was conducted at Center for Nanophase Materials Sciences (CNMS) User Facility, Oak Ridge National Laboratory, which is sponsored by the Office of Basic Energy Science, US Department of Energy. This research is funded by University of California Research Laboratories Grant 09-LR-06-118456-MEYM and National Laser Users Facility Grant PE-FG52-09NA-29043.

- Madhav Reddy K, et al. (2012) Enhanced mechanical properties of nanocrystalline boron carbide by nanoporosity and interface phases. *Nat Commun* 3:1052.
- Thévenot F (1990) Boron carbide—A comprehensive review. *J Eur Ceram Soc* 6(4):205–225.
- An Q, Goddard WA, 3rd (2015) Atomistic origin of brittle failure of boron carbide from large-scale reactive dynamics simulations: Suggestions toward improved ductility. *Phys Rev Lett* 115(10):105501.
- Xie KY, et al. (2015) Atomic-level understanding of “asymmetric twins” in boron carbide. *Phys Rev Lett* 115(17):175501.
- Pavlovskii MN (1971) Shock compressibility of six very hard substances. *Sov Phys Solid State* 12:1736–1737.
- McQueen RG, Marsh SP, Taylor JW, Fritz JN, Carter WJ (1970) The equation of state of solids from shock wave studies. *High-Velocity Impact Phenomena*, ed Kinslow R (Academic, New York), pp 521–568.
- Grady DE (1980) Shock deformation of brittle solids. *J Geophys Res* 85(B2):913.
- Grady DE (1994) Shock-wave strength properties of boron carbide and silicon carbide. *J Phys IV* 4:385–391.
- Grady DE (2015) Hugoniot equation of state and dynamic strength of boron carbide. *J Appl Phys* 117(16):165904.
- Vogler TJ, Reinhart WD, Chhabildas LC (2004) Dynamic behavior of boron carbide. *J Appl Phys* 95(8):4173–4183.
- Zhang Y, et al. (2006) Shock compression behaviors of boron carbide  $B_4C$ . *J Appl Phys* 100(11):113536.
- Holmquist TJ, Johnson GR (2006) Characterization and evaluation of boron carbide for plate-impact conditions. *J Appl Phys* 100:1–13.
- Reddy KM, Liu P, Hirata A, Fujita T, Chen MW (2013) Atomic structure of amorphous shear bands in boron carbide. *Nat Commun* 4:2483.
- Chen M, McCauley JW, Hemker KJ (2003) Shock-induced localized amorphization in boron carbide. *Science* 299(5612):1563–1566.
- Yan XQ, et al. (2009) Depressurization amorphization of single-crystal boron carbide. *Phys Rev Lett* 102(7):075505.
- Ge D, Domnich V, Juliano T, Stach EA, Gogotsi Y (2004) Structural damage in boron carbide under contact loading. *Acta Mater* 52(13):3921–3927.
- Subhash G, et al. (2013) Characterization of the 3-D amorphized zone beneath a Vickers indentation in boron carbide using Raman spectroscopy. *Acta Mater* 61(10):3888–3896.
- Freund LB (1974) Crack propagation in an elastic solid subjected to general loading—IV. Obliquely incident stress pulse. *J Mech Phys Solids* 22(3):137–146.
- Curran D (1987) Dynamic failure of solids. *Phys Rep* 147(5-6):253–388.
- Meyers MA (1994) *Dynamic Behavior of Materials* (John Wiley & Sons, New York).
- Klinger M, Jäger A (2015) *Crystallographic Tool Box (CrystBox)*: Automated tools for transmission electron microscopists and crystallographers. *J Appl Cryst* 48(Pt 6):2012–2018.
- Hýtch MJ, Snoeck E, Kilaas R (1998) Quantitative measurement of displacement and strain fields from HREM micrographs. *Ultramicroscopy* 74(3):131–146.
- Zhao S, et al. (2015) Pressure and shear induced amorphization of silicon. *Extrem Mech Lett* 5:74–80.
- Zhao S, et al. (2016) Amorphization and nanocrystallization of silicon under shock compression. *Acta Mater* 103:519–533.
- Moynihan TJ, LaSalvia JC, Burkins MS (2002) Analysis of shatter gap phenomenon in a boron carbide/composite laminate armor system. *20th International Ballistics Symposium*, eds Carleone J, Orphal D (DEStech Publications, Lancaster, PA), pp 1096–1103.
- Domnich V, Reynaud S, Haber RA, Chhowalla M (2011) Boron carbide: Structure, properties, and stability under stress. *J Am Ceram Soc* 94(11):3605–3628.
- Aryal S, Rulis P, Ching W (2011) Mechanism for amorphization of boron carbide  $B_4C$  under uniaxial compression. *Phys Rev B* 84(18):184112.
- Gust WH, Royce EB (1971) Dynamic yield strengths of  $B_4C$ ,  $BeO$ , and  $Al_2O_3$  ceramics. *J Appl Phys* 42(1):276–295.

